Modeling of Microstructural Kinematics During Simple Elongation of Central Nervous System Tissue

Allison C. Bain

David I. Shreiber

David F. Meaney*

Department of Bioengineering,
University of Pennsylvania,
Philadelphia, PA 19104-6392

Damage to axons and glial cells in the central nervous system (CNS) white matter is a nearly universal feature of traumatic brain injury, yet it is not clear how the tissue mechanical deformations are transferred to the cellular components of the CNS. Defining how cellular deformations relate to the applied tissue deformation field can both highlight cellular populations at risk for mechanical injury, and define the fraction of cells in a specific population that will exhibit damage. In this investigation, microstructurally based models of CNS white matter were developed and tested against measured transformations of the CNS tissue microstructure under simple elongation. Results show that axons in the unstretched optic nerves were significantly wavy or undulated, where the measured axonal path length was greater than the end-to-end distance of the axon. The average undulation parameter—defined as the true axonal length divided by the end-to-end length—was 1.13. In stretched nerves, mean axonal undulations decreased with increasing applied stretch ratio (λ)—the mean undulation values decreased to 1.06 at $\lambda=1.06$, 1.04 at $\lambda=1.12$, and 1.02 at $\lambda=1.25$. A model describing the gradual coupling, or tethering, of the axons to the surrounding glial cells best fit the experimental data. These modeling efforts indicate the fraction of the axonal and glial populations experiencing deformation increases with applied elongation, consistent with the observation that both axonal and glial cell injury increases at higher levels of white matter injury. Ultimately, these results can be used in conjunction with computational simulations of traumatic brain injury to aid in establishing the relative risk of cellular structures in the CNS white matter to mechanical injury. [DOI: 10.1115/1.1632627]

Introduction

The central nervous system (CNS) white matter is composed of myelinated axons, a supporting glial cell network, and an innervating vascular system. Damage to the CNS white matter is a nearly universal consequence of brain and spinal cord injury, and is the largest contributor to poor neurological outcome in survivors of brain and spinal cord trauma [1]. Mechanical strain is considered the proximal cause of injury to the CNS white matter, with secondary ischemic insults potentially exacerbating the initial structural and functional damage that occurs at the moment of injury [2]. Previous work has shown that dynamic stretch of the guinea pig optic nerve—a small, isolated bundle of CNS axons aligned in parallel—produces the same histopathological changes found in white matter injury in humans. Moreover, the guinea pig optic nerve contains the same organotypic architecture of the human optic nerve, and both are considered reasonable representations of white matter tracts within the brain [3].

Although the macroscopic, tissue level deformations for white matter injury are now estimated from work using the guinea pig optic nerve [4], these mechanical thresholds do not allow a precise estimate of the mechanical strains experienced by cellular elements of the white matter. A more precise definition of the relationship between the applied macroscopic conditions during trauma and the resulting cellular deformations under these loads will identify the cell populations that are mechanically at risk for damage, and also highlight the mechanical sensitivity of cells or subcellular elements in the white matter to mechanical trauma. For example, data from in vivo studies of white matter injury show that not all axons are damaged at a fixed level of stretch. At increasing levels of stretch, the relative number of injured axons increases, as does the relative injury to the glial cells surrounding the axonal network [5,6]. Both of these observations suggest a complex recruitment and mechanical loading of axons and glial cells under even simple extension loading. Despite the potential of axonal recruitment on understanding the neuropathology of traumatic axonal injury, though, only one study has examined the kinematics associated with cellular and/or subcellular elements in the white matter during simple mechanical stress states [7]. Although the study demonstrated how the axonal tracts change their geometry during simple loading, a quantitative description relating tensile strain applied to the spinal cord and the resulting geometrical changes in the axons of the white matter were not developed.

Based on the progressive increase in the distribution of axonal and glial injury in white matter tissue with higher levels of applied stretch, we hypothesized that the axons within the white matter become more firmly tethered to the glial cell matrix at higher elongation levels, and that this tethering will be observed by tracking the changes in the axonal microstructure during simple elongation. In this study, we present a mathematical description of the kinematics for axonal deformation in the white matter of the CNS using separate modeling approaches to reflect the potential coupling of the axons to supporting cells within the CNS. We model the microstructural changes that occur in the guinea pig optic nerve under simple extension, a loading condition that is capable of causing white matter injury at sufficiently high elongation rates ($>10\ s^{-1}$) [8]. We show that a gradual coupling of the

*Corresponding address: Department of Bioengineering, 120 Hayden Hall, University of Pennsylvania; Philadelphia, PA, 19104-6392; e-mail: dmeaney@seas.upenn.edu.

Contributed by the Bioengineering Division for publication in the JOURNAL OF BIOMECHANICAL ENGINEERING. Manuscript received by the Bioengineering Division January 14, 2002; revision received June 24, 2003. Associate Editor: M. S. Sacks.

axons to the glial matrix is a more reasonable description than models assuming (a) a uniformly coupled or (b) an uncoupled behavior between the axonal elements and glial matrix fraction across the studied elongation levels. We view this study as the first step in a more detailed description of how the different cell populations in the CNS contribute to the mechanical properties and functional response of the tissue following mechanical stimulation, and will provide a starting point for defining the mechanical tolerance of other cells in the white matter that show damage during brain and spinal cord injury.

Methods

Microstructural Characterization. Adult, male, Hartley, albino guinea pigs (600–700 grams; n=6 animals) were euthanized with a lethal dose of sodium pentobarbital (60 mg/kg), and exsanguinated with 0.1% heparinized saline. Optic nerve length, defined as the distance from the posterior surface of the globe to the optic chiasm, was measured using digital calipers for both the right and left optic nerve prior to removal. Measurements on the axonal microstructure in unstretched nerves from three separate animals showed that the microstructure was not statistically different across animals (Kolmogorov-Smirnov testing; $p>0.5$). Therefore, the data from a stretched optic nerve was not paired with data from the unstretched optic nerve from the same animal. The nerves (n=12 total) were excised and restored to their in vivo length, and the ends of each nerve were pinned to a petri dish. The nerves were then elongated manually at a slow rate (<1 mm/s) once to one of four levels, corresponding to stretch ratios of $\lambda=1.0$ (unstretched), 1.06, 1.12, 1.25. Using enamel markers on the surface of the nerve, separate studies showed that the elongation of the optic nerve produced a reasonably uniform tissue strain along the length of the optic nerve [4]. Moreover, slow loading rates were used to avoid any potential overstretching of the tissue, and minimize potential viscoelastic loading effects. Three separate nerve samples were elongated at each stretch ratio, yielding a total of 12 nerves used for the study. A preliminary power analysis showed that relatively small changes in the average microstructure (e.g., difference of 0.01) could be detected with >95% statistical power using this study design. Once displaced to the final stretch condition, each nerve was fixed with 10% neutral buffered formalin for 24 hours.

Individual nerves were embedded in gelatin and cut on a freezing microtome into longitudinal sections 16 μm thick and stored in phosphate buffered saline (PBS) for no longer than 24 hours. The sections were stained with the antibody SMI 31 (Sternberger Monoclonals, Inc., Baltimore, MD), which stains phosphorylated medium and heavy-weight (160 and 200 kD) neurofilament proteins that are prolific in normal axons, as previously described [9]. In the central nervous system, the neurofilament proteins are the most abundant protein in the axon, and fill the bulk of the axoplasm space. Therefore, labeling of the neurofilaments provides a reasonable estimate of the axonal geometry.

Immunostained nerve sections were mounted on slides, coverslipped, and viewed with light microscopy (Nikon, Inc., Tokyo, Japan) using a 60× objective. Care was taken to ensure that the length of the longitudinal sections were consistent with the measured length prior to cutting on the freezing stage microtome. The optic nerve samples were embedded within gelatin following pinning and fixation but prior to cutting on the microtome, making sure to keep the nerve at its in situ length. By embedding using gelatin and avoiding paraffin embedding, the freezing and cutting process produced no detectable change in the length or diameter of the specimens as measured by calipers.

For each nerve section, approximately sixty images evenly distributed along the length of the nerve section were acquired under bright field microscopy (AIS Image, Imaging Research, Inc., St. Catherines, Ontario) (Fig. 1(*a*)). Five randomly located axonal segments from each of the sixty digital images were chosen for analysis, yielding approximately 300 axonal segments that were

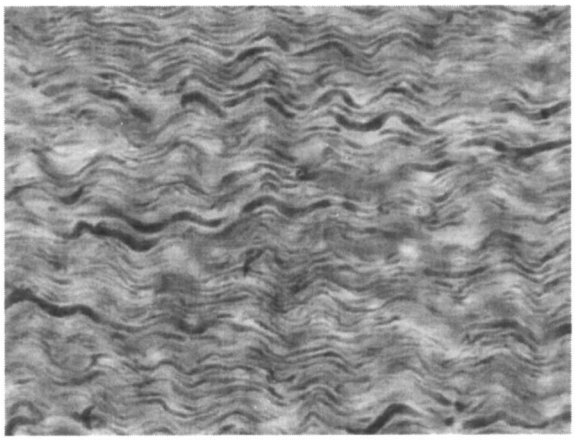

(*a*)

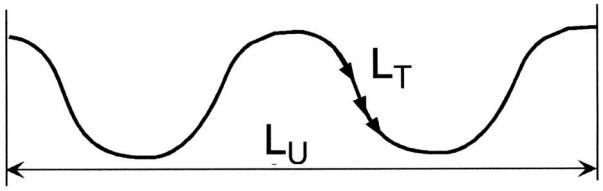

$$U = \frac{L_T}{L_U}$$

(*b*)

Fig. 1 Analysis of the axonal microstructure in the guinea pig optic nerve (*a*) Digital image of an longitudinal optic nerve section stained for non-phosphorylated neurofilament (SMI31 antibody), showing the undulated appearance of individual axons in the nerve. (*b*) Axonal microstructure was described using an undulation parameter (U), based on the end-to-end distance length of an axon (L_U), and the true path length (L_T) of the axon. Undulation parameters closest to 1.0 indicated axons that appeared nearly straight; increasing levels of undulation above 1.0 described axons that were undulated, or 'wavy' in appearance.

characterized for a single nerve sample. These segments were randomly selected from the digital images of the nerve, and represented a distribution of axon caliber within the nerve. Each axon in the digital images was assumed to represent a separate axon in the optic nerve, and the morphology of the axon could be visualized for several undulation cycles. True length (L_T) and undulated (end-to-end) length (L_U) were measured (NIH Image, NIH, Bethesda, MD) (Fig. 1(*b*)) for each axonal segment. The measured undulations of axons from the three separate nerve samples at a specific stretch level were combined into a single dataset for the stretch level. In turn, the resulting dataset at each stretch level was analyzed using a frequency histogram, and the mean undulation for the population was calculated.

To evaluate potential differences in axonal undulation along the length of the nerves within a given stretch level, the nerve was divided into four equal segments and the mean undulation was calculated for each segment. For the three nerves at each stretch level, the average mean undulation was calculated for each of the four regions. For each stretch level, a one-way analysis of variance (ANOVA) (Statistica, Statsoft, Inc., Tulsa, OK) was employed to detect significant differences ($p<0.05$) among the four areas.

Microstructural Modeling. In general, the microstructural components of biological tissues respond to an applied deforma-

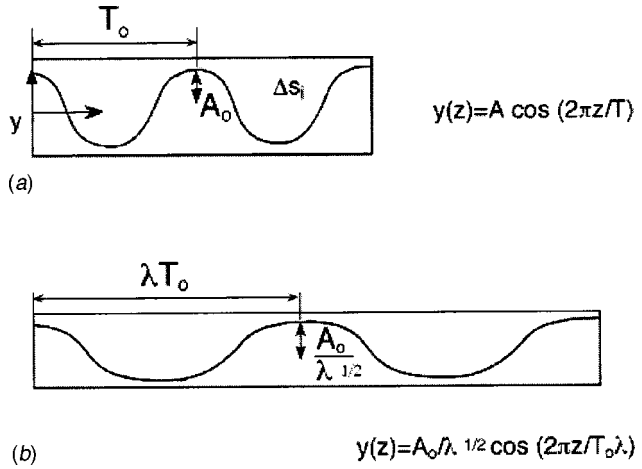

Fig. 2 Schematic depicting the model assuming a tight coupling between the axonal population and the glial cell network. (*a*) The axon path is represented by a periodic wave with amplitude, A_o, and period, T_o. (*b*) When elongated to a stretch ratio of 1, the amplitude of the path decreases to $A_o/\lambda^{-1/2}$, while the path period increases to λT_o. Therefore, both the computed path length and the end-to-end distance of the axon will change for the applied stretch condition, yielding a new undulation value (U_t) that is approximated by the equation shown.

tion based on the interconnectivity of elements at the microscopic level. If the cellular elements are tightly coupled together, one may assume that the cellular elements follow exactly the applied bulk strain pattern (i.e., an affine deformation). In contrast, the cellular elements may have very little connectivity and therefore act independently of each other; the resulting deformation of the cellular elements will not correspond directly with the applied bulk strain field. In this study, we examined three possible transformations for defining how the axons deform within the white matter under simple elongation. These three approaches were based on three different approximations for the coupling between the axonal elements and the supporting glial cells—principally the oligodendrocytes and astrocytes—over the range of stretch conditions examined experimentally.

Complete coupling between axons and glial network—For this approximation, it is assumed that the axons in the optic nerve are tightly interconnected with the glial network, and the axons experience locally the same geometric transformation as the macroscopic tissue. For this analysis, we assumed that the geometry of an undulated axon (y(z)) could be modeled as a periodic wave (Fig. 2(*a*)):

$$y(z) = A_o \cos\left(\frac{2\pi z}{T_o}\right) \tag{1}$$

where A_o is the amplitude of the wave, T_o is the period, and z is the axis along the length of the axon. Assuming incompressibility for the optic nerve, the amplitude and period of an axon under simple extension loading of the tissue become $A_o(\lambda)^{-1/2}$ and $T_o\lambda$, respectively, and the equation of the stretched axon's geometry ($y'(z)$) changes accordingly (Fig. 2(*b*)):

$$y'(z) = \frac{A_o}{\sqrt{\lambda}} \cos\left(\frac{2\pi z}{\lambda T_o}\right) \tag{2}$$

At a point (z) along the length of the axon, the undulation of an axon over a small interval (dz) is given by:

$$U(z) = \sqrt{1+\left(\frac{dy}{dz}\right)^2} \tag{3}$$

The average undulation of the axon (U_o) over a length (L_u) along the axis of the axon is therefore given by:

$$U_o = \frac{1}{L_U}\int_0^{L_u} \sqrt{1+\left(\frac{dy}{dz}\right)^2}\,dz$$

$$= \frac{1}{L_U}\int_0^{L_U} \sqrt{1+\left(-A_o\frac{2\pi}{T_o}\sin\left(\frac{2\pi z}{T_o}\right)\right)^2}\,dz \tag{4}$$

Similarly, for the axon under simple extension loading (λ), the transformed undulation (U_t) becomes:

$$U_t = \frac{1}{L_U}\int_0^{L_u} \sqrt{1+\left(\frac{dy}{dz}\right)^2}\,dz$$

$$= \frac{1}{L_U}\int_0^{L_U} \sqrt{1+\left(\frac{-A_o}{\sqrt{\lambda}}\frac{2\pi}{\lambda T_o}\sin\left(\frac{2\pi z}{\lambda T_o}\right)\right)^2}\,dz \tag{5}$$

There is no closed form solution for Eqs. (4) and (5); as such, we approximated the solutions using a simplification that applies for undulation values close to 1.0. For these undulation values, we used the assumption:

$$(U_{ave})^2 \cong (U^2)_{ave} \tag{6}$$

and therefore,

$$U_{ave} = [(U_{ave})^2]^{1/2} = [(U^2)_{ave}]^{1/2} = \left[\frac{1}{L_U}\int_0^{L_U}\left(1+\left(\frac{dy}{dz}\right)^2\right)dz\right]^{1/2} \tag{7}$$

substituting the equations describing the axonal geometry in the undeformed (Eq. (1)) and deformed (Eq. (2)) into Eq. (7) yielded two separate expressions for the average undulation of an axon over an interval. The two expressions were used to develop a final relationship between the transformed undulation (U_t) and the initial undulation (U_o) based on the stretch ratio applied to the tissue (λ):

$$U_t = U_o\left[\frac{1}{\lambda^3} + \frac{1}{U_0^2}\left(1-\frac{1}{\lambda^3}\right)\right]^{1/2} \tag{8}$$

Numerical integration of Eqs. (4) and (5) for the range of undulations observed in the optic nerve and typical stretch values shows an error from the approximation in Eq. (6) of approximately 0.003 for an undulation value of 1.5 and an applied stretch of 1.25.

No coupling between axonal and glial elements—When the axons within the white matter are assumed to be completely uncoupled with the surrounding cells and matrix, the microstructural transformation is calculated more directly—the undulated length of an axon increases in correspondence to the new displaced length of the nerve, while the true length of the axon remains the same. An axon is completely straight when the nerve stretch ratio (λ) is equal to the axon's original undulation (U_o) (Fig. 3). Therefore, the transformed undulation (U_t) of an individual axon becomes the ratio of L_T to the new undulated length (L_N). U_t can be described at any optic nerve stretch in terms of the nerve stretch ratio and the original undulation of the axon:.

$$U_t = \frac{1}{\lambda}U_o \quad \text{for } \lambda < U_o \tag{9A}$$

$$U_t = 1 \quad \text{for } \lambda \geq U_o \tag{9B}$$

Using this transformation, population averages and statistical distributions can be predicted for a bundle of axons within the optic nerve at any stretch level, given the original population distribution.

Gradual coupling of the glial matrix to the axonal elements—Rather than assuming a local cellular connectivity that applies for all axons within the optic nerve, a final approach is to consider a

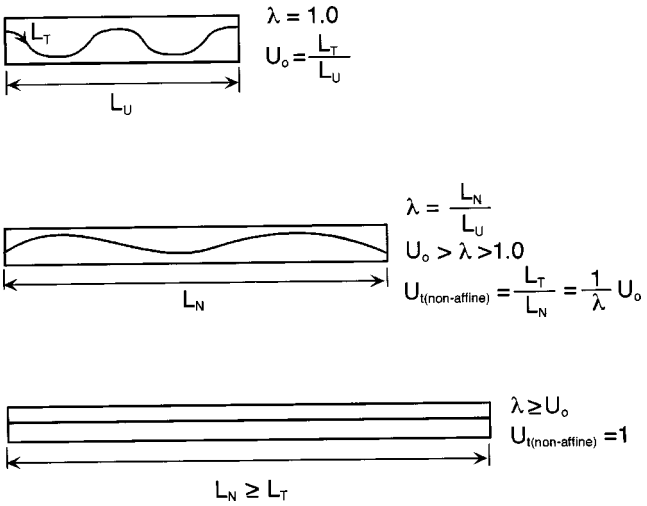

Fig. 3 Schematic depicting the model of axonal microstructure with no coupling to the glial cell network. At stretch ratios less than the axon's undulation value, the applied displacement is transferred directly to increase the axon's end-to-end distance (L_U), with no change in the true path length of the axon (L_T). Therefore, the transformed undulation of the axon after stretch (U_t) is transformed according equation shown. At stretch ratios greater than the original undulation, the axon is completely straight and has an undulation of 1.0.

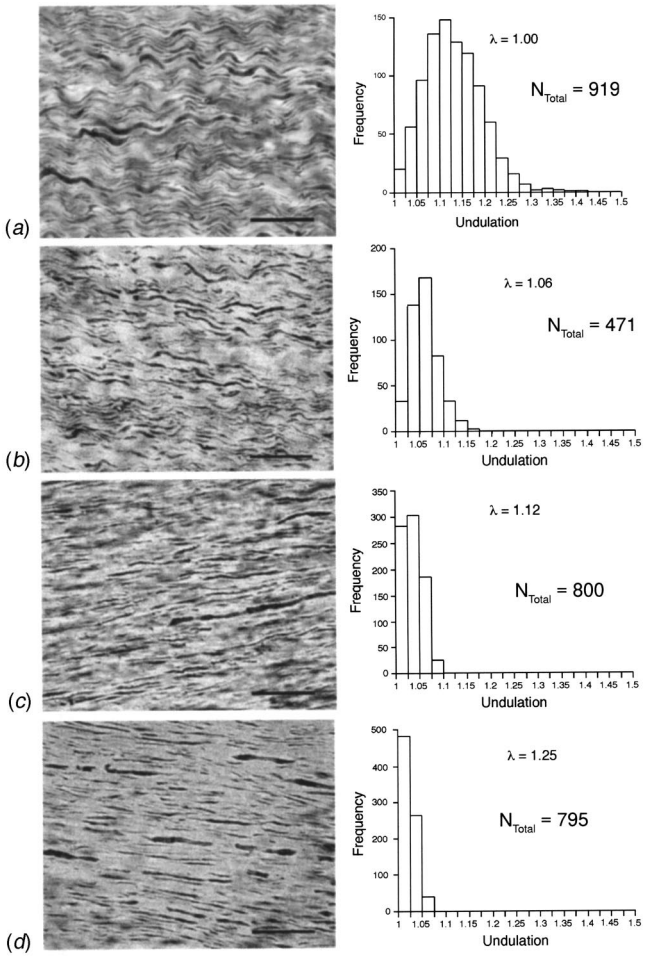

Fig. 4 Measured changes in the axonal microstructure under simple extension. In the resting in situ state (*a*; λ=1.0), axons are compressed and show undulation characteristics across a broad range. At increasing levels of applied tensile stretch (*b–d*), the axonal microstructure changes to a more oriented geometry, with most of the axons appearing nearly straight at the highest level of stretch (*d*, λ=1.25).

situation in which the coupling of the axon to the glial cell matrix changes from an initial uncoupled state to a coupled behavior beyond a specific elongation point. This formulation is an attempt to model the progressive recruitment and damage of the glial cells within the white matter after stretch injury. Each axon will display a unique transition point from uncoupled to coupled behavior. The formal statement of this model is as follows:

For $U < U_1$, all axons are coupled directly to cells and follow the transformation described by Eq. (8),

For $U > U_2$, all axons are not affected by the surrounding glial cell matrix and follow the transformation described by Eqs. (9*A*) and (9*B*), and

For $U_1 < U < U_2$, a unique transition point (U_{tp}) exists for each axon that defines the switch from uncoupled ($U_{uncoupled}$; Eqs. (9*A*)) and (9*B*) to coupled ($U_{coupled}$; Eq. (8) behavior). The transition point is defined separately for each axon, and is randomly assigned between the range from U_1 to U_2. Therefore, the fraction of the axonal population experiencing complete coupling behavior grows linearly as the applied stretch level increases.

Statistical Comparison of Modeling Approaches. To compare the measured changes in axon microstructure with the predictions from the proposed modeling approaches, a statistical test for goodness of fit was used. For each stretch ratio, predictions from the modeling approaches were compared to experimental measurements of the undulation distribution using Kolmogorov-Smirnov (KS) testing [10]. Predicted and measured distributions were considered different for p values less than 0.05.

Results

Microstructural Characterization. The SMI 31 antibody stained optic nerve sections evenly and highlighted many undulated axons under normal light microscopy. Axons were visualized for long distances, suggesting that they follow an in-plane, or 2-D route through the optic nerve. In general, axons were highly aligned along the longitudinal axis in most areas of the nerve, and exhibited areas with little overlap with neighboring axons.

Most axons visualized in unstretched nerves were highly undulated, although calculated undulations ranged from 1.00–1.40 (Fig. 4(*a*)). Undulation histograms showed a relative frequency of nearly zero for undulations of 1.00 in unstretched nerves and generally showed a gradual increase in frequency until undulations of roughly 1.10–1.15. At higher undulations, the frequency of axons tapered slowly, and eventually approached zero. Although the highest undulation calculated was 1.50, few axons (<1%) exhibited undulations greater than 1.33. The mean undulations calculated for the unstretched nerves were not significantly different (Kolmogorov-Smirnov testing, $p > 0.5$). Therefore, the data from the three unstretched nerves were combined into a single distribution with an overall mean undulation of 1.13 (Fig. 4(*a*)).

For unstretched nerves, the mean undulation calculated for the four different regions of the nerve did not vary significantly along the nerve's length. Some nerves exhibited a slightly higher mean undulation in a region near the retina, while the largest mean undulation was observed in the middle region of another nerve. After grouping the three nerves at each level, there were no statistically significant differences among the regional means detected by a one-way ANOVA.

When nerves were elongated to stretch ratios of 1.06, many undulated axons were still visible. However, some axons appeared completely straight and the overall mean undulation of the three grouped nerves at this level subsequently decreased to 1.06. As

expected, the combined frequency distribution shifted noticeably to the left as the average undulation decreased (mean=1.06), with the maximum relative frequency occurring at a much lower undulation level (1.05) and tapering off more quickly (Fig. 4(*b*)).

When nerves were fixed at higher stretch ratios (λ=1.12,1.25), more axons appeared completely straight and few axons were undulated appreciably. At these levels, the combined undulation distribution no longer resembled the initial, unstretched distribution, but rather was similar to an exponential distribution (Figs. 4(*c*) and 4(*d*)). A high percentage of axons had undulations of 1.0, and the distributions quickly decreased to zero at undulations above 1.05. The overall mean undulation decreased to 1.04 at a stretch ratio of 1.12 and to 1.02 at a stretch ratio of 1.25.

Microstructural Modeling. *Complete coupling of the axonal elements to the glial cell matrix*—Assuming the axons are coupled tightly to the surrounding cells at all applied stretch levels, the measured axonal undulations shown in Fig. 4(*a*) were transformed for the three different stretch levels. As stretch levels increased, predicted mean undulation values decreased. However, undulations predicted by this model were considerably higher than those observed experimentally, and the spectrum of predicted undulation values encompassed a range larger than the range measured experimentally (Fig. 5(*a*)). At λ=1.06, the predicted mean undulation was 1.11, much higher than the experimental mean of 1.06. This difference increased at λ=1.12, where the model produced a mean undulation of 1.10 compared to a measured undulation of 1.04, with the disparity continuing at the highest stretch level of λ=1.25, where the predicted mean of 1.07 was considerably higher than the experimentally measured value.

More noticeable differences are observed when examining the cumulative frequency histogram of predicted and observed microstructural changes (Fig. 5(*a*)). Kolmogorov-Smirnov goodness of fit tests showed that none of the predicted distributions matched the measured distributions, each showing significant differences at all stretch ratios. Moreover, a diverging trend was particularly noted in the predictions at higher stretch ratios, with predictions for the highest stretch ratio showing the most marked difference with the measured microstructural characteristics at this level ($p < 0.001$). Although slightly shifted and broadened, the histograms describing the predicted axonal microstructure maintained its shape, resembling a Gamma distribution even at stretch ratios of 1.25.

No coupling between the axonal and glial elements—Assuming the axons are uncoupled to the surrounding glial cell network, the axonal undulations, represented by the distribution shown in Fig. 4(*a*), were transformed for the three different stretch levels using Eqs. (9*A*) and (9*B*). At a stretch ratio of 1.06, the undulation of the axons and the range of undulations predicted by a non-affine deformation were very similar to those observed experimentally, with the mean undulation (1.07) differing only slightly from the experimental mean of 1.06 (Fig. 5(*b*)). At increasing levels of stretch, however, the predicted changes were more pronounced than the measured microstructural parameters. At an applied stretch of 1.12, the predicted mean undulation was 1.02 in comparison to a measured mean of 1.04. At the highest level of applied stretch (λ=1.25), the difference remained approximately the same between measured (1.02) and predicted (1.001) values of the mean undulation.

The shape of the measured cumulative frequency distribution differed from the predicted distribution using a complete coupling behavior, and showed a slightly better match to the experimental data at the lowest elongation level (Fig. 5(*b*)). However, Kolmogororv-Smirnov goodness of fit tests showed that none of the predicted undulation distributions matched the measured populations at any of the stretch levels. With the assumption of no coupling between the glial cell matrix and the axonal elements, the predicted distributions quickly shifted to show a large fraction of axons at low undulation values, changing the predicted shape of the distribution to resemble more of an exponential shape. The shape difference in the histograms describing measured and predicted axonal microstructure decreased at higher stretch ratios, with both predicted and measured displaying similar shapes at the highest stretch level of 1.25.

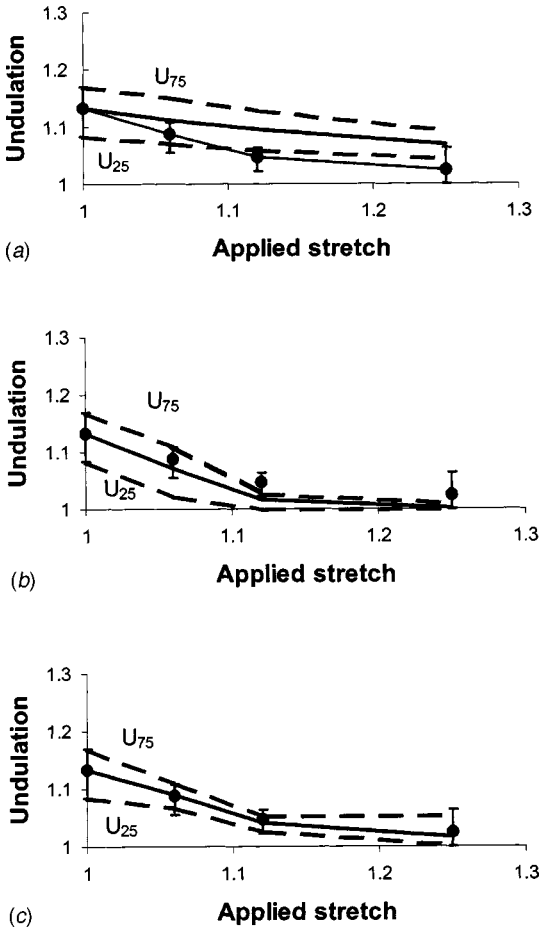

Fig. 5 Predicted (lines) and measured (symbols) changes in the axonal microstructure. Models assuming either a complete coupling to glial matrix (*a*) or an absence of coupling of the glial matrix (*b*) during simple extension do not follow either the average undulation values or the distribution of undulation values measured in stretched optic nerves (symbols). Additionally, the distribution of undulation values measured in stretched optic nerves, described with the 25th and 75th percentile values (bars), were not predicted well with either of these two models (dashed lines). (*c*) A more accurate prediction of the average undulation, as well as the spread in the distribution of the undulation values, was found using a model that assumed a gradual recruitment of the glial cell matrix at lower undulation values (*c*).

Gradual coupling of the glial matrix to the axonal elements—Using a transformation that models the graded recruitment or tethering of the glial matrix to the axonal elements, the original unstretched population of axons was transformed according to the relationships described earlier. The limits defining the transition to complete coupling behavior (U_1) and the regime of completely uncoupled behavior (U_2) were defined by the response of the model across all stretch ratios by minimizing the difference between the predicted and measured changes in the population. With limits established (U_1=.98; U_2=1.08), the model was compared to measured changes in the microstructure. Across all stretch levels, the mean undulations predicted from this model matched the measured values well, showing no significant difference at any of the applied stretch levels ($p>0.15$).

The shape of the cumulative frequency histogram predicted

from this gradual transformation model matched best the measured data on axonal geometry during simple elongation (Fig. 5(*c*)). Kolmogorov-Smirnov testing showed no significant difference between the measured and predicted changes at all levels of stretch, unlike the two models described earlier. The span of the frequency distribution followed the experimental trend at all stretch levels (Fig. 5(*c*)), and changed to an exponential shape at the highest stretch level, much like the experimental distribution.

Discussion

In this investigation, we studied how a macroscopic strain field applied to a white matter tract, the guinea pig optic nerve, results in the deformation of the underlying axonal microstructure by comparing analytical descriptions of the transformation to an experimental characterization of the nerve. We determined that optic nerve axons in the unstretched state are undulated to varying degrees, and that the axonal microstructure changed significantly as the optic nerve was elongated. Our major finding supported our hypothesis that a transitional mechanics model—which described an initial uncoupled deformation phase for the axons within the glial matrix that is followed by an increasingly affine or coupled deformation phase—best represents the axonal microstructure changes as the optic nerve is subject to simple extension.

The appearance of the axonal microstructure in the spinal cord during normal neck flexion and extension has been reported previously [7]. The results from this past study show the undulated appearance of the axons in full-neck extension, with the microstructure straightening noticeably when the neck was placed in full flexion. No attempts to quantify either the strain in the spinal cord or the microstructure during these maneuvers was conducted. The results in this paper represent the first detailed quantification of the undulated nature of the CNS microstructure and its transformation under applied loading. Clearly, the importance of the microstructural characteristics of biological tissue, and its corresponding role in structure-property relationships for the tissue, has been studied for other soft tissues [11–14]. Applying these principles to the white matter will allow the development of similar structure-property-function relationships that can be applied to understand the response of the white matter to mechanical forces that are both physiological and non-physiological (e.g., traumatic injury and growth) in nature.

In this analysis, we recognize that the validity of our data ultimately relies on the quality of our methods and techniques. Although there are many effective ways to visualize axonal projections, there were several advantages to using neurofilament antibody immunohistochemistry. Nerves could be excised and fixed in vitro without losing their antigenicity and could be viewed under light microscopy. By identifying a major unit of the cytoskeletal network (i.e., the neurofilaments), the axonal microstructure was more directly observable and did not need to be estimated using other techniques, such as staining for myelin basic protein. Effects of tissue shrinkage were also considered, as these may affect microstructural geometry. Shrinkage effects were mitigated by pinning the ends of the nerve during fixation, and by avoiding paraffin-embedding, which often contributes to tissue shrinkage through a series of hydration/dehydration steps. No detectable change in width was observed in the transverse direction, and the lengths of the slide-mounted nerve sections were never less than the measured in vivo lengths. Moreover, because artifact due to these procedures is rarely reproducible, the repeatability of our measurements across nerve sections at a fixed in vitro elongation level suggested shrinkage was not a significant error in our measurements. Finally, any quantification of immunohistochemical results may not be clear because the quality of the stain is often inconsistent between nerves or between different areas of a single nerve. However, each nerve resulted in 30–35 evenly and uniformly stained sections from which we chose our sections for analysis. Consequently, we believe that our results were not affected by inconsistent staining.

The relationship between the microstructural components of the CNS and the deformation applied to the tissue provides a useful insight into the pathophyisological response of the white matter to stretch, as well as potential implications for a stress-stretch relationship for the white matter. A previous study has shown that only a small fraction of the axons in the white matter will display any abnormal pathology following stretch, although this fraction of injured axons will increase as the injury severity increases [8]. The nonuniform patterns of axonal pathology parallels the heterogeneous transfer of applied deformation predicted from our analytical description. At a given level of tissue stretch, all axons are not deformed the same amount. Rather, the axonal population displays a range of stretch conditions. Based on recent in vitro studies using cultured CNS axons, it is likely that only the axons that experience the highest levels of stretch will show a pathophysiological response [15]. The fraction of axons above this pathophysiological stretch threshold increases proportionally with the level of applied tissue stretch, therefore increasing the fraction of injured axons or 'severity' of the injury at higher levels of stretch. In addition, the increasing recruitment of axons and glia at higher levels of stretch suggests a strongly nonlinear stress-stretch behavior for the white matter. Recent studies suggest that there is a marked nonlinearity of brain tissue in shear [19], some of which could be explained by the microstructural changes.

Significant limitations of this study include the potential damage and load transfer problems associated with the pinning technique to elongate the samples, the slow elongation of the samples in contrast to the rapid rates used to cause axonal injury, and the post-mortem condition of the tissue. First, although care was taken to ensure that the pins are attached firmly into the tissue prior to elongation, no quantification of the local strain field surrounding the pins was made in this study. Although none of the tissue sections showed noticeable tearing at the pin attachment site, the applied strains noted in this study are approximated as the overall applied strains and do not represent local strain measures. Second, the slow elongation protocol was used to ensure that final displacement condition was reached, but not exceeded. Additionally, concerns regarding tissue tearing at higher rates could be minimized with the slower rate. Therefore, these data do not explicitly model the microstructure changes that can occur during the higher rates ($\sim$1–10 s^{-1}) associated with axonal injury. Finally, the tissue was tested as rapidly as possible following removal to minimize any post-mortem effects. No noticeable signs of tissue degradation were observed in the tissue sections, and no signs of primary axotomy were observed in any of the tissue samples.

The microstructural models not only allow one to better assess the underlying mechanisms and tolerance for axonal pathology, but also provide possible insight into the relative risk of the glial cellular structures to injury following dynamic stretch. Although we considered the possibility of simple frictional forces among axons that could induce the transition from uncoupled to coupled behavior, interactions between axons and other components in the white matter were a more likely explanation due to the characteristics of the cellular architecture. For example, a single oligodendrocyte—the myelin-producing glial cell of the CNS—myelinates several axon segments, and many oligodendrocytes are required to fully myelinate an axon. Therefore, the network of oligodendrocytes may act mechanically as crosslinks that affect the kinematic behavior of nerve. Clearly, the mechanical properties and geometry of the oligodendrocytes will affect the transition, or cross-linking point, between coupled and uncoupled behavior. The randomized transition point used in the mixed formulation approach is an approximation of the difference in the mechanical properties and geometry for the population of oligodendrocytes, but likely does not model completely the factors that define this transition process. Nevertheless, the results from the mixed formulation approach suggest the oligodendrocytes will sense the applied mechanical load at higher elongation levels, and

therefore may be at risk for primary mechanical injury. It is worth noting that recent studies in brain and spinal cord injury show an acute oligodendrocyte response after mechanical injury in support of these predictions, with an increase in the severity of white matter injury corresponding to an increasing amount of oligodendrocyte damage [5,6].

Finally, with the additional insight into how applied strain fields are reflected in the deformation of the axonal microstructure, it is now possible to use this analysis and link the mechanical thresholds established at the tissue level for the guinea pig optic nerve to many different regions of the human CNS. Combined with an examination of the microstructure of anatomical areas such as the corpus callosum, the internal radii, or the spinal cord, the current results can be scaled appropriately to define the specific mechanical parameters necessary to cause injury in these areas. These results will be particularly useful for finite element analyses that are capable of defining mechanical response of the brain to impact loading [16–18], but lack the regional tolerance information to determine the relative proportion of the white matter that will be injured for a specified impact. Using measurements of microstructure across different brain regions to determine microscopic mechanical thresholds for white matter injury, it will become feasible to predict both the severity and extent of diffuse axonal injury (DAI) that would occur in a given impact situation. Together, these efforts could significantly enhance the understanding of the conditions that cause white matter injury in man and lead to the development of better safety technologies to mitigate the incidence of DAI in the population.

Acknowledgments

Funds for this work were provided by CDCR49/CCR312712, NIH R01 N535712 and NIH R01 HD41699.

References

[1] Gentleman, S. M., Roberts, G. W., Gennarelli, T. A., Maxwell, W. L., Adams, J. H., Kerr, S., and Graham, D. I., 1995, ''Axonal Injury: A Universal Consequence of Fatal Closed Head Injury?'' Acta Neuropathol. (Berl), **89**(6), pp. 537–543.

[2] Graham, D. I., Adams, J. H., Nicoll, J. A., Maxwell, W. L., and Gennarelli, T. A., 1995, ''The Nature, Distribution and Causes of Traumatic Brain Injury,'' Brain Pathol., **5**(4), pp. 397–406.

[3] Waxman, S. G., Kocsis, J. D., and Stys, P. K., 1995, *The Axon: Structure, Function, and Pathophysiology*, New York: Oxford University Press. 682.

[4] Bain, A. C., and Meaney, D. F., 2000, ''Tissue-Level Thresholds for Axonal Injury in an Experimental Model of CNS White Matter Injury,'' J. Biomech. Eng., **122**, pp. 615–622.

[5] Crowe, M. J., Breshnahan, J. C., Shuman, S. L., Masters, J. N., and Beattie, M. S., 1997, ''Apoptosis and Delayed Degeneration After Spinal Cord Injury in Rats and Monkeys,'' Nat. Med., **3**(1), pp. 73–76.

[6] Grossman, S. D., Rosenberg, L. J., and Wrathall, J., 2001, ''Temporal-Spatial Pattern of Acute Neuronal and Glial Loss After Spinal Cord Contusion,'' Exp. Neurol., **168**(2), pp. 273–282.

[7] Breig, A., 1960, Biomechanics of the Central Nervous System, Stockholm: Almqvist & Wiksell. 183.

[8] Bain, A. C., Raghupathi, R., and Meaney, D. F., 2001, ''Dynamic Stretch Correlates to Both Morphological Abnormalities and Electrophysiological Impairment in a Model of Traumatic Axonal Injury,'' J. Neurotrauma, **18**(5), pp. 499–512.

[9] Sternberger, L. A., and Sternberger, N. H. 1983, ''Monoclonal Antibodies Distinguish Phosphorylated and Nonphosphorylated Forms of Neurofilaments in Situ,'' Proceedings of the National Academy of Science, USA, **80**, pp. 6126–6130.

[10] Zar, J., 1984, Biostatistical Analysis, 2nd edition. Upper Saddle River, NJ: Prentice Hall.

[11] Rigby, B., Hirai, N., Spikes, J., and Eyring, H., 1959, ''The Mechanical Properties of rat Tail Tendon,'' J. Gen. Physiol., **43**, pp. 265–283.

[12] Viidik, A., 1968, ''A Rheological Model for Uncalcified Parallel-Fibered Collagenous Tissue,'' J. Biomech., **1**, pp. 3–11.

[13] Lanir, Y., 1979, ''A Structural Theory for the Homogeneous Biaxial Stress-Strain Relationships in Flat Collagenous Tissues,'' J. Biomech., **12**, pp. 423–436.

[14] Billiar, K., and Sacks, M., 1997, ''A Method to Quantify the Fiber Kinematics of Planar Tissues Under Biaxial Stretch,'' J. Biomech., **30**(7), pp. 753–756.

[15] Smith, D. H., Wolf, J. A., Lusardi, T. A., Lee, V. M. Y., and Meaney, D. F., 1999, ''High Tolerance and Delayed Elastic Response of Cultured Axons to Dynamic Stretch Injury,'' J. Neurosci., **19**(11), pp. 4263–4269.

[16] Zhang, L., Yang, K. H., and King, A. I., 2001, ''Comparison of Brain Response Between Frontal and Lateral Impacts by Finite Element Modeling,'' J. Neurotrauma, **18**(1), pp. 21–30.

[17] Ruan, J. S., Khalil, T., and King, A. I., 1994, ''Dynamic Response of the Human Head to Impact by Three-Dimensional Finite-Element Analysis,'' J. Biomech. Eng., **116**, pp. 44–50.

[18] Bandak, F. A., Eppinger, R. H., and DiMasi, F., 1996, ''Assessment of Traumatic Brain Injury Using Automotive Crash Tests and Finite Element Analysis,'' in: *AGARD Head Injury Specialist Meeting*, Mescalero, NM.

[19] Prange, M. T., and Margulies, S., 2002, ''Regional, Directional, and Age-Dependent Properties of the Brain Undergoing Large Deformation,'' J. Biomech. Eng., **24**, 244–253.